ACS OMEGA

http://pubs.acs.org/journal/acsodf

Article

Reversible Oxidation Quantified by Optical Properties in Epitaxial $Fe_2CrO_{4+\delta}$ Films on (001) $MgAl_2O_4$

Mark D. Scafetta, Tiffany C. Kaspar, Mark E. Bowden, Steven R. Spurgeon, Bethany Matthews, and Scott A. Chambers*

Cite This: *ACS Omega* 2020, 5, 3240−3249

Read Online

ACCESS | Metrics & More | Article Recommendations | Supporting Information

ABSTRACT: We report on the structural and optical properties of $Fe_2CrO_{4+\delta}$ epitaxial films grown by molecular beam epitaxy on $MgAl_2O_4$ (001) as a function of δ (average cation valence). The average Fe valence is linked to the out-of-plane lattice parameter and the extent of light absorption in the infrared spectral region. Over-oxidized films ($0 < \delta < 0.5$) exhibit smaller lattice parameters and suppressed infrared absorption. The lattice parameter is found to differ for films of equivalent oxidation state but different thermal histories. We discuss the behavior of a novel infrared transition present at ∼0.6 eV in Fe_2CrO_4 films deposited at or above 400 °C. An optical transition found in all films at 0.9 eV independent of the synthesis temperature can be used to quantify the oxidation state of $Fe_2CrO_{4+\delta}$. This research provides new insights into the atomic structure, optical processes, oxidation states, electronic structure, and application potential of $Fe_2CrO_{4+\delta}$.

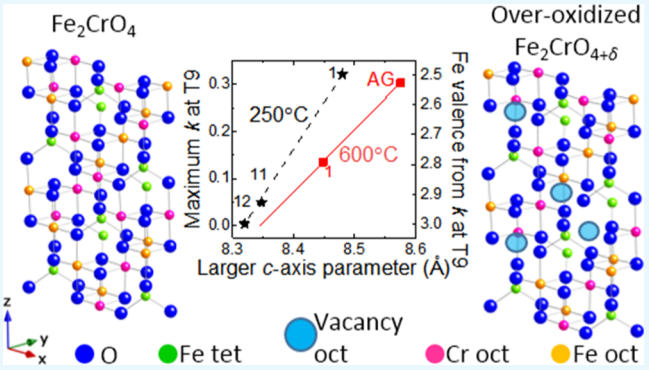

INTRODUCTION

$Fe_2CrO_{4+\delta}$ exhibits attractive optical, electronic, and magnetic properties which make it potentially useful for energy conversion, magnetic memory, and spintronic applications.[1−4] However, it is not known how this material behaves as a function of the oxygen content (δ). Understanding material properties as a function of the oxidation state, especially for transition-metal oxides, is of utmost importance. It is common to misinterpret material properties because the assumed oxidation state has not been confirmed by measurements. Quantifying the oxidation state of a thin-film sample can be difficult. We discuss a process adapted from other transition-metal oxides[5−7] to easily quantify the oxidation states in $Fe_2CrO_{4+\delta}$.

Fe_2CrO_4 is compositionally half way between the mineral end members Fe_3O_4 (magnetite) and $FeCr_2O_4$ (chromite). Oxygen-stoichiometric Fe_2CrO_4 is the only intermediate compound that has been previously targeted and analyzed for its functional properties. Fe_2CrO_4 is a semiconductor that absorbs visible light and exhibits photoconductivity.[3] It is a ferrimagnet with a Curie temperature well above ambient.[3] These functional properties are expected to depend on cation valences as they do in Fe_3O_4 (magnetite)[8,9] and other materials.[6,10,11] Stoichiometric Fe_2CrO_4 exhibits a spinel crystal structure with equal concentrations of Fe^{2+} and Fe^{3+}, resulting in an average Fe valence of 2.5.[3,4] Cr was previously observed to exclusively occupy octahedral sites in Fe_2CrO_4,[3] in agreement with the very large stabilization energy for Cr^{3+} in octahedral coordination.[12] Fe occupies all of the tetrahedral and remaining octahedral sites of the spinel structure.[3] Over-oxidation of Fe_2CrO_4 to $Fe_2CrO_{4+\delta}$ is accommodated by continuous cation vacancy formation until 100% of Fe is converted to Fe^{3+} ($\delta = 0.5$) and forms a cation-deficient spinel phase analogous to γ-Fe_2O_3 (maghemite).[13] Smooth, monotonic changes in the lattice parameter are expected with increasing oxidation in the spinel phase.[8,13,14] A corundum phase analogous to α-Fe_2O_3 (hematite) can also form at higher oxidation temperatures.[15,16]

The over-oxidation process in $Fe_2CrO_{4+\delta}$ is expected to terminate when all Fe cations have a valence of 3+ ($\delta = 0.5$, $Fe_2CrO_{4.5}$). Fe^{4+} (or $Fe^{3+}L$, where L is a ligand hole) is typically only found in lattices containing a stable 2+ cation such as Sr^{2+}[17−20] or Ni^{2+}.[21,22] When exposed to conditions known to form Fe^{4+} in Sr^{2+}- and Ni^{2+}-containing materials, Fe^{4+} is not found in materials lacking a 2+ cation.[5,23] The average Fe valence in Fe_2CrO_4 does not appear to drop below +2.5 upon reduction, indicating that oxygen vacancies (V_O) do not readily form in Fe_2CrO_4, limiting the average oxidation

Received: October 5, 2019
Accepted: February 3, 2020
Published: February 14, 2020

https://dx.doi.org/10.1021/acsomega.9b03299
ACS Omega 2020, 5, 3240−3249

Table 1. Systematic Annealing Sequence Used to Probe Oxidation and Reduction of $Fe_2CrO_{4+\delta}$ Epitaxial Films

deposition temp (°C)	anneal number	annealing environment	temp (°C)	pressure (Torr)	duration (h)	large/small c values (Å)	SE(S) XPS(X)
250	AG						X
	red-1	MBE, vac		1×10^{-8}	0.2	8.480/8.304	S,X
	ox-2	TF, air	190	ambient	2.0		S
	ox-3	TF, air	200	ambient	8.0		S
	ox-4	TF, air	200	ambient	20.0		S
	ox-5	TF, O_2	200	ambient	15.0		S
	ox-6	UV/O_3	ambient	ambient	1.0		S,X
	ox-7	MBE, plasma	200	4×10^{-5}	10.0		X
	red-8	MBE, vac	200	1×10^{-8}	22.0		X
	red-9	MBE, vac	225	1×10^{-8}	11.0		X
	red-10	MBE, vac	225	1×10^{-8}	12.0		X
	ox-11	MBE, plasma	200	4×10^{-5}	3.0	8.348/8.216	S,X
	ox-12	TF, O_2	400	ambient	1	8.320/8.200	S
600	AG					8.575/8.512	S,X
	ox-1	HP, air	250	ambient	2.5	8.447/8.375	S

[a]AG = as-grown. Red = anneals that are expected to produce a lower oxidation state than the previous condition. ox = anneals that are expected to produce a higher oxidation state than the previous condition. MBE, vac = vacuum annealing ($P \leq 1 \times 10^{-8}$ Torr) in the MBE chamber. MBE, plasma = annealing in a beam of activated oxygen from an electron cyclotron plasma oxygen source in the MBE chamber at $P = \sim 4 \times 10^{-5}$ Torr. TF, air = annealing in a tube furnace in air at ambient pressure. TF, O_2 = annealing in a tube furnace with flowing pure O_2 at 1 atm. (flow rate = 0.2 L/min). UV/O_3 = exposure to simultaneous ozone and UV light in a Jelight UV/ozone cleaner. HP = annealing on a hot plate in air with the sample placed on clean Si wafer and an inverted alumina crucible placed over the sample as a protective lid. The large and small c lattice parameter values come from the split (004) Bragg reflections. The small (large) c values are determined from the large (small) Bragg angles. SE = spectroscopic ellipsometry. XPS = X-ray photoelectron spectroscopy.

range from Fe^{3+} to $Fe^{2.5+}$ ($\delta = 0.5$ to $\delta = 0$, $Fe_2CrO_{4.5}$ to Fe_2CrO_4).[13]

The oxidation states of the cations are extremely important properties and optical absorption characteristics are a powerful way to determine them. It is possible to quantify the average Fe oxidation state in $Fe_2CrO_{4+\delta}$ using the static imaginary part (dielectric function [ε_2], extinction coefficient [k], or absorption coefficient [α]) of its optical constants.[5,7,24] X-ray photoemission spectroscopy (XPS) is commonly used to estimate oxidation states, but this can be a daunting task for ferrites (due to multiplet splitting of the Fe 2p peak) and only probes the top ∼5 nm of the material. In magnetite, the Verwey transition temperature is routinely used to estimate the oxidation state, but this process is rather qualitative and can be influenced by factors other than oxidation state changes.[25,26] Lattice parameters can be useful to estimate the oxidation state for many materials, but a strong dependence on the strain state and/or defect concentration can make comparisons between different samples difficult or impossible. The optical properties of ferrites provide a quantitative method for determining the average oxidation state throughout the entire film for thicknesses in excess of 5 nm. Differences in strain and defect concentrations are generally found to result in minor changes in a material's optical properties relative to the large changes induced by variations in cation valence.[6,27]

A detailed analysis of the optical properties as a function of changing oxidation state has not previously been presented for $Fe_2CrO_{4+\delta}$. Many of the optical transitions in materials related to $Fe_2CrO_{4+\delta}$ (and other transition-metal compounds) are dependent on the relative amounts of Fe^{3+} and Fe^{2+} (and other transition-metal oxidation states) in the lattice.[28−33] Therefore, significant changes in the optical spectra are expected when changing the oxidation state(s) in $Fe_2CrO_{4+\delta}$. Here, we compare the structural and optical properties of epitaxial films of $Fe_2CrO_{4+\delta}$ on $MgAl_2O_4(001)$ as a function of the extent of over-oxidation and synthesis conditions. This research will shed light on the relationships between the oxidation state(s), atomic structure, and optical properties in $Fe_2CrO_{4+\delta}$. Potential improvements in synthesis parthways and the utility of $Fe_2CrO_{4+\delta}$ will also be discussed.

EXPERIMENTAL SECTION

Fe_2CrO_4 films of thickness 120 to 400 Å were deposited on 10 mm × 10 mm × 0.5 mm, (001)-oriented, $MgAl_2O_4$ (MAO) substrates (CrysTec GmbH) via molecular beam epitaxy (MBE) as described elsewhere.[4] In order to determine the influence of growth temperature on the oxidation processes and resulting properties, we focus in this study on two of the previously studied samples,[4] one film is deposited at 250 °C and another at 600 °C. These films were previously determined to be stoichiometric within the uncertainty of XPS.[4] We subjected the samples to the annealing conditions outlined in Table 1. This set of anneals was designed to sequentially over-oxidize and reduce MBE-grown films in a controlled way in order to systematically investigate reversible oxidation/reduction in $Fe_2CrO_{4+\delta}$ films.

In situ XPS was carried out on as-deposited and vacuum annealed films. Ex situ XPS data were also collected after annealing samples outside of the UHV system. Samples for ex situ analysis were cleaned for 5 min in a Jelight ultraviolet/ozone cleaner, which removes most of the carbon contamination, before reintroduction into the vacuum system. Carbon contamination was found only after reintroducing cleaned samples into the XPS/MBE system (e.g., after anneal ox-6, as shown in Table 1). Carbon was undetectable after anneal ox-7, which was carried out in the MBE chamber.

XPS was performed using a VG/Scienta R3000 analyzer with monochromatic Al Kα X-rays. All spectra were shifted to align the O 1s peak to 531.0 eV, except the Fe and Cr 2p spectra, as shown Figure 1a−c, measured after deposition, and after the first in situ annealing at 250 °C. For these spectra, an electron flood gun was required to neutralize the charging effects. The spectral dispersion of the analyzer is slightly

https://dx.doi.org/10.1021/acsomega.9b03299
ACS Omega 2020, 5, 3240−3249

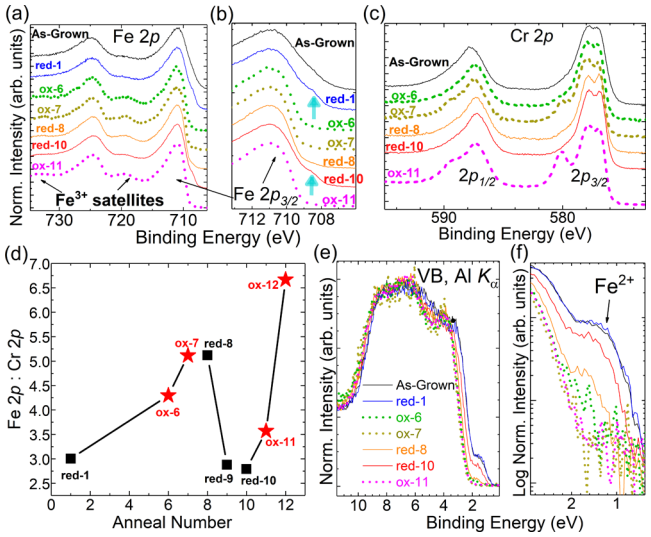

Figure 1. Normal emission XPS spectra for a representative as-grown film, and after anneals summarized in Table 1. Thick dashed lines represent anneals expected to result in increased oxidation compared to the previous condition. Thin solid lines represent as-grown or anneals expected to decrease oxidation state compared to the previous condition. (a) The complete Fe 2p spectra and (b) magnified region of the Fe $2p_{3/2}$ feature. Vertical arrows highlight the shoulders from Fe^{2+}. (c) Cr 2p spectra for the same anneals. (d) Fe 2p/Cr 2p as a function of the annealing condition. Stars represent anneals that are expected to be oxidizing relative to the previous condition and squares are anneals that are expected to be reducing compared to the previous condition. (e) Valence band spectra and (f) enlarged region of the VB near 2 eV on a logarithmic scale.

different when the flood gun is on compared to when it is off. For this reason, the Fe and Cr 2p spectra, as shown in Figure 1a–c, for the sample deposited at 250 °C in the as-grown condition, and after anneal red-1 (see Table 1), were shifted to align the Fe $2p_{3/2}$ peak with that measured after anneal red-10, as shown in Table 1.

Film thickness and roughness were determined by X-ray reflectivity (XRR). Out-of-plane (OOP) *c*-axis lattice parameters were measured by X-ray diffraction (XRD) and are listed in Table 1. All XRD and XRR data were collected using the same instrumentation (PANalytical X'Pert Materials Research Diffractometer) described previously,[4] except for the annealed sample deposited at 600 °C. Data from this sample were collected using a Rigaku SmartLab diffractometer with a rotating Cu anode operated at 45 kV and 200 mA. The incident beam (Cu Kα) was filtered using a two-bounce Ge(220) monochromator. OOP θ–2θ scans employed a matching monochromator for the diffracted beam. Reciprocal space maps were converted to direct space maps (DSMs) for convenience and were recorded without an analyzer monochromator and utilizing a HyPix 3000 detector operating in line-detection mode.

Optical properties were measured within the spectral range of 0.5–4.6 eV using spectroscopic ellipsometry (J.A. Woollam V-VASE). Data were collected using at least three incident angles spanning 40–75°. Ellipsometry fits were obtained by determining the refractive index (n) and extinction coefficient (k) of the modeled layer that best reproduced the ellipsometry data, using a model consisting of the layer thickness and roughness from XRR as inputs. An exception was made for the model generated from the as-grown film deposited at 250 °C. For this sample, XRR yielded a surface roughness of ∼2.5 nm which led to a model generating unrealistically sharp features in the UV region after fitting. The roughness measured after anneal ox-11 (Table 1) was 1 nm. This value was used in the model for the as-grown 250 °C film and yielded reasonable line shapes. Relatively small changes occur in the resulting spectra by further reducing the roughness to 0 nm. Others have shown that XRR yields greater values for roughness compared to atomic force microscopy and ellipsometry.[34,35] Roughness can also be caused by surface adsorbates,[36] which can have significantly different optical properties and densities compared to the underlying film. The effect of these adsorbates on XRR and ellipsometry measurements may not be comparable. Additionally, if XRR and ellipsometry were conducted with a significant amount of time between them, the absorbate layer coverage and thickness can be different from one sample to another. Additional details of the film synthesis, XPS, XRD, XRR, and ellipsometry data collection and analysis, can be found elsewhere.[4]

Lift-outs for cross-sectional scanning transmission electron microscopy (STEM) were prepared for both samples. The data for the film deposited at 600 °C were previously presented, and the preparation and imaging methods are reported elsewhere.[4] STEM samples from the film deposited at 250 °C were prepared using a standard lift out process on a FEI Helios DualBeam 660 focused ion beam microscope, with initial cuts performed at 30 kV and final thinning at 2 kV ion milling energy. Imaging was performed on a probe-corrected JEOL GrandARM-300F microscope operating at 300 kV, with a convergence semi-angle of 29.7 mrad and an inner collection angle of 75 mrad. Energy-dispersive X-ray spectroscopy (STEM–EDS) maps were collected using a dual JEOL Centurio detector setup (∼1.6 sr solid angle), with a 1 Å probe size, ∼237 pA probe current, and 10 μs px^{-1} dwell time.

RESULTS

Chemical and Structural Analysis. Figure 1a–f shows XPS spectra at different stages of annealing. The Fe 2p spectra (Figure 1a,b) have been used as qualitative indicators of the Fe valence.[37] The satellite features from Fe^{2+} and Fe^{3+} between the main Fe $2p_{3/2}$ (∼711 eV, as shown in Figure 1) and Fe $2p_{1/2}$ (∼725 eV, as shown in Figure 1) spin–orbit features are of similar intensity in Fe_3O_4.[38] This leads to a filling of the valley between the main Fe 2p spin–orbit features. The main Fe $2p_{3/2}$ and $2p_{1/2}$ features shift slightly to higher binding energies with increased over-oxidation. Figure 1b shows the low binding energy shoulder in the Fe $2p_{3/2}$ feature highlighted by vertical arrows. This shoulder becomes less pronounced after oxidizing anneals and is well known to originate from Fe^{2+}.[39] However, strong overlap between the features associated with Fe^{3+} and Fe^{2+} makes it difficult to quantify the relative amounts of the two Fe valences using the Fe 2p spectrum.[9]

Figure 1c shows high-resolution Cr 2p spectra. The line shapes and binding energies are largely consistent with Cr^{3+}. However, characteristic peaks appear at ∼580.5 and ∼590 eV after annealing in O plasma (anneals ox-7 and ox-11 in Table 1). This behavior has previously been tentatively attributed to the presence of a double surface chromyl (Cr═O) termination after exposure to the O plasma.[40] The peaks at ∼580.5 and ∼590 eV shrink after reducing anneals. The multiplet splitting of Cr $2p_{3/2}$ has been previously shown in Fe_2CrO_4 and is consistent with that measured for α-Cr_2O_3.[3]

https://dx.doi.org/10.1021/acsomega.9b03299
ACS Omega 2020, 5, 3240–3249

A decrease of the Cr 2p peak area was observed after relatively oxidizing anneals, as seen in Figures 1d and S7. This behavior was previously reported in bulk polycrystalline samples of several ferrites, including Fe_2CrO_4 and $FeCr_2O_4$, and is consistent with the formation of cation vacancies and Fe segregation to the surface during oxidation.[41] The preferential segregation of Fe to the surface during oxidation was related to the differences in Fe and Cr diffusivity at temperatures below ~600 °C, driven by the relative oxidation potentials of Fe^{2+} and Cr^{3+}.[42] The estimated relative surface compositions after annealing range from $Fe_{2.15}Cr_{0.85}O_{4+\delta}$ to $Fe_{1.86}Cr_{1.14}O_{4+\delta}$, and are estimated to be precise within ~±3%. However, these values are only within an error of ~±10% of the absolute composition.[42]

The VB spectra, as shown in Figure 1e,f, provide additional insights into the over-oxidation process. The entire spectrum shifts to slightly higher binding energy with increased over-oxidation, consistent with the Fermi level moving away from the VB. At the same time, the Fe^{2+} peak at ~1.5 eV binding energy becomes weaker with increasing over-oxidation, as expected.[39] Based on the absence of the Fe^{2+} VB feature, anneal ox-11 results in the greatest extent of over-oxidation according to XPS. Judging from the fact that the intensity at ~1.5 eV after reducing anneals is not as large as that in the as-grown case, the most reducing anneal (anneal red-10 in Table 1) did not restore Fe_2CrO_4 to its as-grown state. Thus, removing all excess oxygen from $Fe_2CrO_{4+\delta}$ is difficult under the conditions we explored. This result is consistent with previous reports that did not detect oxygen vacancies in Fe_2CrO_4 after reducing anneals.[13] The O 1s spectra for the film deposited at 250 °C after the various anneals are shown in Figure S1. The only significant change results from surface hydroxyl contaminants[43] after reintroduction from ambient into the XPS chamber. However, this species desorbs after anneal ox-7.

The OOP XRD patterns for the 250 °C film as-deposited and after anneal ox-12 are displayed in Figure 2a. Figure 2b shows the XRD OOP diffraction pattern in the as-grown state for the film deposited at 600 °C, and after annealing in air at 250 °C for 2.5 h. The OOP XRD scan from 15 to 85° (2θ) can be found in Figure S2, and shows no additional peaks other than {001}-related features from the substrate and film. The splitting of the film (004) Bragg peak, which is attributed to Cr and Fe segregation,[4] is present in the as-grown state and after all anneals in both samples. An increase in the (004) Bragg peak splitting relative to that of the as-grown material is observed in Figure 2b. This change after annealing the 600 °C film in air at 250 °C for 2.5 h (condition 1 for the 600 °C film in Table 1). This result indicates that annealing at 250 °C leads to increased Cr/Fe segregation, in agreement with previous reports.[41] The OOP Bragg peak splitting for the film deposited at 250 °C remains nearly constant, even after annealing at 400 °C (anneal ox-12 in Table 1). Interestingly, the oxidation power of anneal ox-11 which was done using the O plasma source in the MBE, is weaker than that of anneal ox-12, carried out at ambient pressure in an O_2 tube furnace, as determined by the smaller lattice parameter achieved after the latter. According to XPS, the film after anneals ox-12 and ox-11 appears to be fully oxidized and the spectra are similar to those of hematite[26,44] The discrepancy between XPS, which indicates complete oxidation after anneal ox-11, and XRD, which indicates incomplete oxidation, is related to the different probe depths of these techniques (~5 nm for XPS vs the entire film depth for XRD). Annealing in O plasma (ox-11) appears to fully oxidize the near-surface region, but not the entire film, whereas the tube furnace anneal (ox-12) is sufficient to fully oxidize the entire film.

By comparing the d_{xy} parameters for the film and substrate, partial strain is observed in the film deposited at 600 °C, as shown in Figure 2c. Annealing has little effect on the strain, as shown by the invariant d_{xy} values before (Figure 2c) and after annealing (Figure 2d). A clear shift to smaller d_z is observed with increasing over-oxidation, in agreement with the OOP scans, as shown in Figure 2a,b, and previous reports on bulk lattice parameters.[13] The physical cause is a decrease in the Fe−O bond length resulting from the increased Coulomb attraction associated with increased Fe valence.

Optical Properties. The optical properties of the film deposited at 250 °C before and after a series of anneals are shown in Figure 3a,b. Figure 4a,b shows the optical properties of the film deposited at 600 °C before and after annealing,

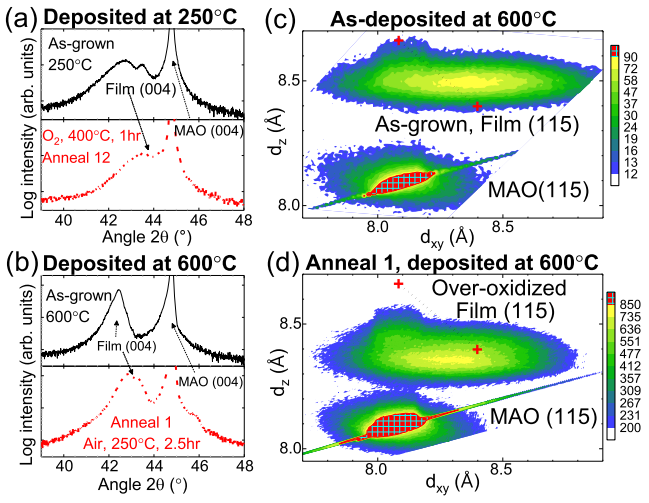

Figure 2. XRD for films grown at (a) 250 and (b) 600 °C in the as-grown, stoichiometric (top) and over oxidized (bottom) states. (c) Direct space map (DSM) for an as-grown film deposited at 600 °C. (d) DSM for the film deposited at 600 °C after annealing for 2.5 h in air at 250 °C (ox-1). The crosses represent the expected pseudomorphic and relaxed lattice parameters for stoichiometric Fe_2CrO_4.[4]

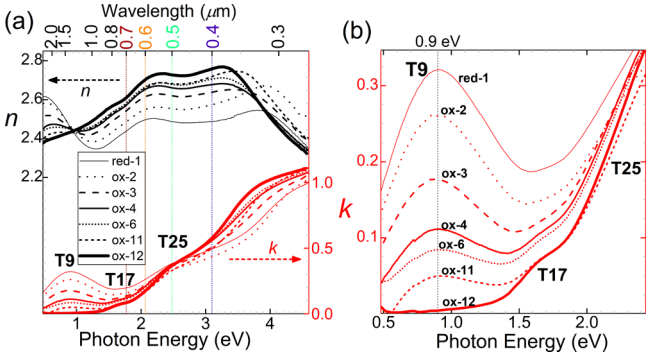

Figure 3. (a) Refractive index (n) and extinction coefficient (k) for epitaxial Fe_2CrO_4 in the as-grown state and after several anneals for a film deposited at 250 °C. (b) Magnified extinction coefficient (k) in the lower photon energy range. The numbers correspond to the annealing conditions in Table 1.

https://dx.doi.org/10.1021/acsomega.9b03299
ACS Omega 2020, 5, 3240−3249

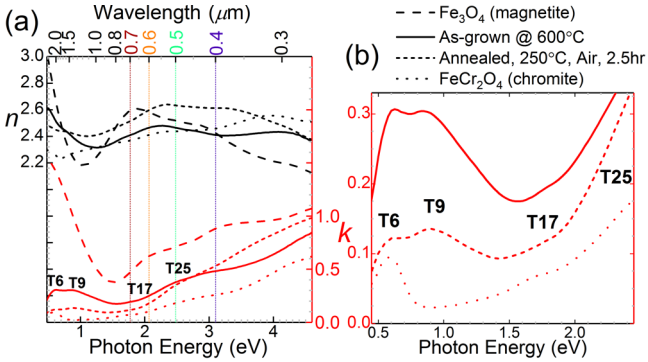

Figure 4. (a) Refractive index (n) and extinction coefficient (k) before and after oxidation for a film deposited at 600 °C. Films of Fe_3O_4 and $FeCr_2O_4$ on (001) MAO are also included. (b) Magnified extinction coefficient (k) in the lower photon energy range. The anneal (ox-1) of the film deposited at 600 °C was over-oxidizing relative to the as-grown state.

along with reference spectra from Fe_3O_4 and $FeCr_2O_4$ epitaxial films deposited on (001) MAO. Cr substitution for Fe leads to systematic changes, as evidenced by comparing spectra for $FeCr_2O_4$, Fe_2CrO_4, and Fe_3O_4, seen in Figure 4. More pronounced transitions and higher extinction coefficients in the visible region are observed with increasing over-oxidation.

The extinction coefficient near 0.9 eV (T9) becomes smaller and eventually undetectable with increasing over-oxidation, as seen in Figure 3. An absorption peak near 0.6 eV (T6) is absent from all spectra collected from the film deposited at 250 °C (Figure 3) but is present for the film deposited at 600 °C. The optical constants for the film deposited at 600 °C show a slightly faster decrease in T6 compared to T9 with increasing over-oxidation, as shown in Figure 4. T9 and T6 are directly correlated with the intensity of the Fe^{2+} VB peak, as shown in Figure 1e. Comparing Figures 3 and 4, some broad absorption between 0.9 and 1.4 eV is found in $FeCr_2O_4$[45] that is not observed in the most over-oxidized $Fe_2CrO_{4+\delta}$ sample deposited at 250 °C after anneal ox-12.

In Figure 3b, an absorption peak near 1.7 eV (T17) is readily observed in the most oxidized (anneal ox-12, Table 1) $Fe_2CrO_{4+\delta}$ spectrum for the film deposited at 250 °C. T17 is present in all spectra except that of Fe_3O_4 but becomes somewhat obscured in samples with a relatively reduced average Fe valence. T17 is slightly more visible for the as-grown film deposited at 600 °C compared to the film deposited at 250 °C, as seen by comparing the as-grown spectra, as shown in Figures 3b and 4b. This is consistent with improved structural quality in the 600 °C film resulting in less broadening. T17 has a similar extinction coefficient ($k \approx 0.08$) in $FeCr_2O_4$ (Figure 4) and in the most oxidized $Fe_2CrO_{4+\delta}$ spectrum (anneal ox-12), as shown in Figure 3.

The absorption edge associated with the peak near 2.5 eV (T25) systematically becomes steeper and shifts to higher energy with increased over-oxidation, as observed in Figures 3 and 4. However, the magnitude of the extinction coefficient of T25 is largely invariant with changes in the extent of over-oxidation of $Fe_2CrO_{4+\delta}$. T25 is stronger in $Fe_2CrO_{4+\delta}$ than in $FeCr_2O_4$, and weaker than in Fe_3O_4 (Figure 4). Increased spectral weight is observed above 2.5 eV as the material is oxidized. The highest transition edge captured, near 3.5−4 eV, redshifts with increasing over-oxidation. Evidence of a higher-lying transition becomes visible in the over-oxidized samples. Difference optical spectra for the most oxidized minus the most reduced (as-grown) samples are shown in the Figures S3 and S4, along with the difference spectra for magnetite minus chromite.

DISCUSSION

Our overall data set can be integrated to yield insights into these redox processes in the following way. We start by plotting the magnitude of the extinction coefficient at T9 as a function of the OOP lattice parameter, as shown in Figure 5a.

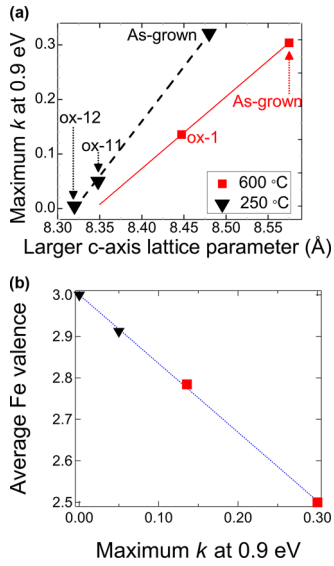

Figure 5. (a) Magnitude of the extinction coefficient (k) at peak T9 (~0.9 eV) versus the OOP c-axis lattice parameter for $Fe_2CrO_{4+\delta}$ films deposited at 250 and 600 °C after various anneals (see Table 1). The linear fits assume that the lattice parameter for a given film is a linear function of the degree of oxidation. (b) Average Fe valence of Fe_2CrO_4 films deposited at 250 and 600 °C as a function of the magnitude of the extinction coefficient (k) at peak T9. A linear regression of the data points is shown as a dotted line.

The OOP lattice parameter is a good quantitative indicator of the extent of over-oxidation for a given film, if the lattice parameter of at least one end-member (stoichiometric Fe_2CrO_4 with $Fe^{2.5+}$, fully oxidized $Fe_2CrO_{4.5}$ with Fe^{3+}, or both) is known. However, different behaviors are observed with over-oxidation for films with different initial lattice parameters, which precludes using the OOP lattice parameter as a universal measure of the extent of oxidation. The differences in lattice parameter behavior are related to the growth conditions, atomic structure, defect concentration, epitaxial strain, and cation oxidation state (δ) of the film. This result is manifested by the dissimilar slopes of the two lines, as shown in Figure 5a, which is related to the different strain states and/or different atomic structures obtained at different deposition temperatures for Fe_2CrO_4 films on (001) MAO.[4] The relative strain states in these two samples possibly differ, but this cannot be verified directly because of the lack of a DSM feature for the 250 °C film.[4] Based on the differences in optical properties, namely, the presence of the T6 absorption feature for the 600 °C film only, we suspect a difference in the atomic structure may also contribute to different lattice parameters at different synthesis temperatures.

Making the assumption that the as-grown samples contain stoichiometric $Fe^{2.5+}$ (this was previously confirmed for the

https://dx.doi.org/10.1021/acsomega.9b03299
ACS Omega 2020, 5, 3240−3249

600 °C film[4] by X-ray absorption near-edge spectroscopy, XANES), and "250 °C ox-12" is fully oxidized (Fe^{3+}), the Fe valence of the intermediate points (250 °C ox-11 and 600 °C ox-1) can be estimated assuming a linear relationship between the Fe valence and lattice parameter for each data set.[6,7] In Figure 5b, these Fe valences are plotted as a function of the magnitude of the extinction coefficient at T9. Despite the differences in the lattice parameter, these points lie nearly on a single line when correlated with the extinction coefficient at T9. A linear regression produces a best-fit line of the form [Fe valence] = 1.66([T9]) + 3.00, where [Fe valence] is the average Fe valence in Fe_2CrO_4, and [T9] is the magnitude of the extinction coefficient at T9 (~0.9 eV). Using this relationship to quantitatively estimate δ in $Fe_2CrO_{4+\delta}$ does not require prior knowledge of the OOP lattice parameter or sample thermal history. As a further advantage, the extinction coefficient can be measured with nondestructive optical techniques that are readily available in many laboratories, unlike other quantitative measures of valence such as XANES.

The difference in the as-grown lattice parameter and slope of the fit lines, as shown in Figure 5a, can be used to indirectly indicate strain. Yearian et al.[13] have previously measured bulk lattice parameters for stoichiometric and over-oxidized $Fe_2CrO_{4+\delta}$. The stoichiometric material value is ~8.40 Å and the over-oxidized material yields ~8.37 Å, resulting in a difference of ~0.03 Å. Based on estimates of the Poisson's ratio (~0.28 for magnetite[46] and ~0.3 for maghemite[47] and realizing that Cr has a minor effect as outlined in our previous work[4]), the OOP *c*-axis lattice parameter for a pseudomorphic, stoichiometric Fe_2CrO_4(001) film would be ~8.66 Å under biaxial compression from an (001) oriented MAO substrate. The analogous pseudomorphic lattice parameter of the over-oxidized $Fe_2CrO_{4+\delta}$ (001) film would be ~8.60 Å leading to a difference of 0.06 Å. This difference in the *c*-axis lattice parameter is twice as large for the strained system than the bulk (relaxed) system. Therefore, we conclude that the film deposited at 250 °C is more relaxed than the film deposited at 600 °C, based on the weaker dependence of the OOP lattice parameter on the extent of over-oxidation, as shown in Figure 5. This is a very useful result because we previously found that Fe_2CrO_4 films deposited ≤250 °C on MAO do not exhibit a (115) DSM Bragg peak, precluding direct analysis of the strain state of the film.[4]

The extent of oxidation in the over-oxidized sample was not determined in Yearian, et al.[13] However, the net change in oxidation is irrelevant for the strain analysis in the previous paragraph. We are only comparing qualitative changes in the lattice parameter with relative changes in oxidation, which helps to determine the strain state.

As with the XRD data, the Fe valence differs slightly between estimates generated using T9 absorption and estimates using XPS. This can be observed by comparing the data in Table 1 with Figures 1−4 after anneal ox-11. Minimal Fe^{2+} character is observed in the Fe 2p and VB spectra after oxygen plasma anneals ox-7 and ox-11, as shown in Figure 2. However, the T9 absorption still exhibits signatures of Fe^{2+} after anneal ox-11 (T9 absorption is not minimized). As with the XRD results, the discrepancy between XPS and ellipsometry is due to the different probe depths for the two techniques. Ellipsometry probes the entire ~40 nm film. Using XPS, ~85% of the signal is obtained from the top ~4.6 nm (~5.5 unit cells) of the material.[48] Therefore, analysis of oxidation extent via XPS is only representative of the entire film for films under ~5 nm thick.

In Fe_2CrO_4, the relatively narrow energy width of T6 is consistent with a tetrahedral Fe^{2+} single-ion d−d crystal field absorption process as previously determined for $FeCr_2O_4$[28,45,49] and similar materials with tetrahedral Fe^{2+}.[28,29] T6 is present only in $Fe_2CrO_{4+\delta}$ films deposited at ≥400 °C,[4] independent of the average Fe valence, as shown in Figures 3 and 4. T6 scales with oxidation, analogous to T9, which indicates that T6 and T9 both involve transitions from the Fe^{2+} VB feature, as shown in Figure 1e,f.

It was previously shown that T6 increases with increasing OOP lattice.[4] T6 appears only in $Fe_2CrO_{4+\delta}$ films that approach the pseudomorphic strain state at growth temperatures ≥400 °C. The strain behavior of the optical properties was previously compared for Fe_2CrO_4 films deposited at ~250 °C on MgO and MAO.[4] Neither film exhibited T6, but both films were deposited at a temperature at which T6 did not develop when depositing on MAO.[4] The absence of T6 in spectra for films deposited at ≤250 °C, independent of strain, suggests that these films do not contain Fe^{2+} at tetrahedral sites. This observation suggests that the degree of inversion is influenced by the substrate temperature during deposition, favoring inverse spinel at lower temperatures. However, previous studies found Fe^{2+} at the tetrahedral sites in films deposited on MgO under similar conditions.[3] This result highlights the effect that subtle differences in synthesis conditions, such as deposition temperature, can have on the degree of spinel inversion (normal vs inverse) in Fe_2CrO_4. The relationship between synthesis conditions and degree of inversion has not been widely studied in the iron spinels, and our results suggest that Fe_2CrO_4 thin films may serve as an interesting model system for future studies.

Fe^{2+} nominally occupies octahedral sites in $Fe_{0.93}O$ and Fe_3O_4. The single-ion Fe^{2+} crystal field transition in $Fe_{0.93}O$[50] and Fe_3O_4[51] is shifted to higher energies near ~0.9 eV compared to ~0.6 eV for tetrahedral Fe^{2+} compounds like $FeCr_2O_4$. This is a result of the stronger crystal field surrounding octahedral sites compared to tetrahedral sites.[28,29,45,52,53] Fe_3O_4 exhibits a somewhat smaller shift than $Fe_{0.93}O$.[50,51] This difference is consistent with a mixture of inverse and normal spinel structures in Fe_3O_4.[54] The mixture of Fe^{3+} and Fe^{2+} at tetrahedral and octahedral sites leads to a mixture of the transitions associated with such cations, resulting in broadened absorption features. Considering the significant admixture between normal and inverse spinel structures in Fe_2CrO_4,[3] we suspect that the inverse-normal spinel mixture contributes significantly to the breadth of T9.

The difference in the magnitude of the extinction coefficient of the crystal field single-ion Fe^{2+} transition at ~0.9 eV between $Fe_{0.93}O$ and $FeCr_2O_4$ can be explained by the approximately three times higher Fe^{2+} concentration in $Fe_{0.93}O$ compared to $FeCr_2O_4$. Fe_3O_4 has the same Fe^{2+}concentration as $FeCr_2O_4$ and Fe_2CrO_4, so in principle Fe_3O_4 should exhibit the same magnitude of extinction coefficient at 0.9 eV as these oxides, but instead Fe_3O_4 has nearly the same T9 absorption as $Fe_{0.93}O$.[50,51] This result has been interpreted as "intensification," which occurs when aliovalent Fe atoms exist at neighboring lattice sites.[28,30−32] According to this criteria, the Fe_2CrO_4 films measured here could have absorption contributions at ~0.9 eV because of intensification.

https://dx.doi.org/10.1021/acsomega.9b03299
ACS Omega 2020, 5, 3240−3249

Changing the degree of spinel inversion should alter the extinction coefficient of a transition experiencing "intensification," by changing the concentration of aliovalent cations at neighboring lattice sites. Based on their different lattice parameters and distinctly different T6 behaviors, we suggest that the films discussed here show evidence for different degrees of inversion. Thus, we expect to observe a difference in the extinction coefficient between these films for a transition exhibiting "intensification". However, the maximum extinction coefficient at 0.9 eV is ∼0.3 for all deposition temperatures of Fe_2CrO_4, as displayed in Figures 3 and 4 and shown in our previous research.[4] The similarities in the T9 extinction coefficient, independent of the degree of inversion, suggest that intensification does not play a significant role at T9 in our films.

T9 absorption monotonically decreases in $Fe_2CrO_{4+\delta}$ as δ increases, indicating that T9 is related to Fe^{2+}. Considering that XPS shows complete oxidation after anneal ox-11 and ellipsometry shows nearly complete oxidation after anneal ox-11 (again with the discrepancy being related to different probe depths), this monotonic decrease in the extinction coefficient at ∼0.9 eV is approximately linear with the change in the Fe valence. This linear behavior further suggests that intensification is not significant in $Fe_2CrO_{4+\delta}$ and is consistent with T9 being a single-ion crystal field transition from the highest occupied octahedral Fe^{2+} 3d state to the lowest unoccupied Fe 3d state.[50,51] Figure 4 shows slight absorption at 0.9 eV in $FeCr_2O_4$ (chromite), which can be explained by the overlapping tails of T6 and T17, or by a slight excess of Fe in the film. T9 is strongly enhanced in Fe_3O_4, as shown in Figure 4. Thus, we suggest that T9 in $Fe_2CrO_{4+\delta}$ requires octahedral Fe^{2+}, which is formally absent from pure $FeCr_2O_4$.

While the oxidation dependence of the extinction coefficient at T9 for $Fe_2CrO_{4+\delta}$ is approximately linear and suggestive of a single-ion process, the compositional dependence of the extinction coefficient at T9 with decreasing Cr content from $FeCr_2O_4$ to Fe_3O_4 is not linear, indicating that "intensification" eventually begins to play a role at some point within this phase space. T9 does not have the exact same dependence on extent of over-oxidation as does T6. Therefore, exchange coupled pairing or intervalence charge transfer cannot be ruled out as a secondary process contributing to T9 in $Fe_2CrO_{4+\delta}$.[29] Further discriminating between and describing these absorption processes requires detailed local structural analysis, polarization-dependent optical characterization, temperature-dependent measurements, and magneto-optical experiments, which are beyond the scope of this paper.

Analyzing the changes in optical properties to estimate oxidation extent is not unique to $Fe_2CrO_{4+\delta}$. Other Fe systems show similar behavior. Substituting Sr for La in $La_{1-x}Sr_xFeO_{3-\delta}$[6,7,19] yielded comparable changes in optical properties to those observed here after subjecting samples by reducing/oxidizing anneals.[6] The same effect with chemical substitution is also expected in $Fe_2CrO_{4+\delta}$. For example, substituting Mg^{2+} cations for Fe^{2+}, leading to a larger fraction of Fe^{3+}, should produce an effect similar to that of oxidation. We expect that this method can be extended to allow for cation valence estimation in other Fe based and non-Fe-based oxide systems.

Considering that the XPS revealed a change in the Fe/Cr cation ratio at the surface (Figures 1d and S7), we analyze the possibility that segregated layering or cation grading affects the associated optical properties. To this end, we introduced various surface layers and gradients into our optical model. The results can be seen in Figure S6. None of these models significantly modify the behavior of the extinction coefficient at low energy. Therefore, assuming a single optical layer for the Fe_2CrO_4 film is a reasonable approximation.

We address the possible difference in optical properties resulting from a difference in cation segregation profiles within the bulk of the film by analyzing cross-sectional STEM−EDS maps, as shown in Figure S5. In Figure S5, we observe a similar microstructure for both films in the as-grown state, indicating that there is no dependence of cation segregation behavior on growth temperature, at least in the 250 to 600 °C range. Previous reports have suggested cation homogenization at ≥600 °C;[41] however, we previously detected Mg (<1 atomic %) diffusion from the MgO substrate to the surface of the film deposited at 600 °C. Attempts to deposit at a higher temperature may result in less Fe and Cr cation segregation but will also result in more Mg diffusion from the substrate into the film. Based on the similar microstructures between the films deposited at 250 and 600 °C, the significant difference in optical properties (namely the transition at 0.6 eV) is not a result of the relatively small degree (∼10%) of chemical segregation observed, but likely results from the different atomic structures (measured as a difference in the OOP *c*-axis lattice parameter) that arise from a different degree of spinel inversion induced by different synthesis temperatures.

Material quality may be improved by modifying the growth conditions such that over-oxidized $Fe_2CrO_{4+\delta}$ (δ = 0.5) is condensed during synthesis. Postgrowth annealing under reducing environments can then be used to achieve the desired oxygen stoichiometry. $Fe_2CrO_{4.5}$ has a smaller lattice parameter than the O-stoichiometric phase, making the lattice match between the film and MAO substrate more favorable. Oxygen-stoichiometric (δ = 0) $Fe_2CrO_{4+\delta}$ is also relatively complex, containing Fe^{3+} and Fe^{2+} at tetrahedral and octahedral sites.[3] This allows for a large possible variance in the degree of spinel inversion, which may account for many of the unique observations in this system. $Fe_2CrO_{4.5}$ only contains +3 cations and does not allow for any variance in the degree of spinel inversion, greatly simplifying the lattice. Another benefit of eliminating +2 cation sites is that Mg^{2+} diffusion may be suppressed, allowing for increased growth temperatures without Mg contamination from the substrate and potentially leading to improved crystallization and compositional homogeneity.

General material properties can be deduced from the obtained optical spectra. The lack of absorption below ∼1.4 eV in over oxidized $Fe_2CrO_{4+\delta}$ may improve the material as a solar absorber relative to stoichiometric Fe_2CrO_4. Additionally, the absorption coefficient across the visible and UV region of the electromagnetic spectrum is enhanced with increasing δ in $Fe_2CrO_{4+\delta}$.

SUMMARY

The chemical, structural, and optical properties of $Fe_2CrO_{4+\delta}$ films grown on $MgAl_2O_4$(001) have been characterized as a function of extent of over-oxidation. Several reversible trends are observed in XPS spectra, including the modulation of an Fe^{2+}-derived feature at the top of the valence band near 1.5 eV, which drops as δ increases. The OOP lattice parameter decreases with increasing δ in our films. The relative trends in the OOP lattice parameter with oxidation suggest that films deposited at 250 °C and below are more relaxed than films

https://dx.doi.org/10.1021/acsomega.9b03299
ACS Omega 2020, 5, 3240−3249

deposited at temperatures ≥400 °C. The value of the OOP lattice parameter is found to be a poor indicator of the oxidation state between films with different thermal histories but is useful in estimating the extent of over-oxidation for a given sample.

The average Fe valence, determined by δ in $Fe_2CrO_{4+\delta}$, is inversely related to the magnitude of the extinction coefficients at ∼0.6 eV (T6) and ∼0.9 eV (T9). As reported earlier, T6 is only observed in films deposited at ≥400 °C,[4] but is not induced solely as a result of a difference in the oxidation state. T6 results from a thermally induced structural change, most likely the occupation of tetrahedral sites by Fe^{2+}, which is apparently absent from films deposited at ≤250 °C. This result highlights the complex roles that synthesis temperature and oxidation state have in activating electronic/optical processes in these materials. Thus, extreme care must be taken to properly synthesize and analyze materials and compare their properties, especially when considering films and bulk materials, and samples with different thermal histories.

The intensities of T6 (where relevant) and T9 are directly related to the highest energy VB feature near 1.5 eV, which is known to be Fe^{2+}-derived, and their magnitudes should trend closely for films less than 5 nm thick. For thicker films, the level of over-oxidation (δ) throughout the film thickness can easily be estimated from the extinction coefficient at ∼0.9 and ∼0.6 eV (if applicable). Changing microstructures as a result of annealing do not have a significant influence on the optical properties compared to inducing changes in Fe oxidation state.

The strain state of $Fe_2CrO_{4+\delta}$ can be determined from the change in lattice parameter as a function of oxidation. Strained films exhibit a faster change in lattice parameter with oxidation compared to relaxed films. This is particularly useful for films deposited at 250 °C and below, which do not exhibit diffraction from (115) planes.

$Fe_2CrO_{4+\delta}$ exhibits minimal absorption below ∼1.2 eV when over oxidized. Fe_2CrO_4 may be useful for applications requiring a tunable infrared absorption coefficient. Higher oxidation states may lead to potentially favorable optical properties for solar energy conversion, marked by weaker IR, and stronger UV/visible light absorption with increasing over-oxidation.

■ ASSOCIATED CONTENT

Supporting Information

The Supporting Information is available free of charge at https://pubs.acs.org/doi/10.1021/acsomega.9b03299.

O 1s XPS for the film deposited at 250 °C after various anneals; OOP XRD θ−2θ scans for films deposited at 250 and 600 °C, before and after postannealing; refractive index difference between the most and least oxidized films; extinction coefficient difference between the most and least oxidized films; STEM−EDS images and line profiles for films grown at 250 and 600 °C; modeled optical properties for the film deposited at 250 °C; Fe 2p, Cr 2p XPS normalized to constant O 1s intensity for the film deposited at 250 °C after various anneals; optical extinction coefficient dependence on photon energy for various films deposited on $MgAl_2O_4$(001); and XPS survey spectra for the film deposited at 250 °C as grown and after annealing in air at 400 °C (PDF)

■ AUTHOR INFORMATION

Corresponding Author

Scott A. Chambers − *Physical and Computational Sciences Directorate, Pacific Northwest National Laboratory, Richland 99532, Washington, United States;* orcid.org/0000-0002-5415-043X; Email: sa.chambers@pnnl.gov

Authors

Mark D. Scafetta − *Physical and Computational Sciences Directorate, Pacific Northwest National Laboratory, Richland 99532, Washington, United States;* orcid.org/0000-0003-3637-6475

Tiffany C. Kaspar − *Physical and Computational Sciences Directorate, Pacific Northwest National Laboratory, Richland 99532, Washington, United States;* orcid.org/0000-0003-2816-7569

Mark E. Bowden − *Environmental Molecular Sciences Laboratory, Pacific Northwest National Laboratory, Richland 99532, Washington, United States*

Steven R. Spurgeon − *Energy and Environment Directorate, Pacific Northwest National Laboratory, Richland 99532, Washington, United States;* orcid.org/0000-0003-1218-839X

Bethany Matthews − *Energy and Environment Directorate, Pacific Northwest National Laboratory, Richland 99532, Washington, United States*

Complete contact information is available at: https://pubs.acs.org/10.1021/acsomega.9b03299

Funding

This research was supported by the U.S. Department of Energy (DOE), Office of Basic Energy Sciences, Division of Materials Science and Engineering under award no. 10122.

Notes

The authors declare no competing financial interest.

■ ACKNOWLEDGMENTS

This research was supported by the U.S. Department of Energy (DOE), Office of Basic Energy Sciences, Division of Materials Science and Engineering under award no. 10122. This research was performed at the W. R. Wiley Environmental Molecular Sciences Laboratory, a DOE User Facility sponsored by the Office of Biological and Environmental Research and located at the Pacific Northwest national Laboratory (PNNL). PNNL is a multiprogram national laboratory operated for DOE by Battelle. STEM sample preparation was performed in the Radiological Microscopy Suite (RMS), located in the Radiochemical Processing Laboratory (RPL) at PNNL.

■ REFERENCES

(1) Lee, D. S.; Chern, G. Electrical Transport Properties of $Fe_{3-x}Cr_xO_4$ Ferrite Films on MgO (001) Grown by Molecular Beam Epitaxy. *Phys. B* **2012**, *407*, 297−301.

(2) Robbins, M.; Wertheim, G. K.; Sherwood, R. C.; Buchanan, D. N. E. Magnetic Properties and Site Distributions in the System $FeCr_2O_4$-Fe_3O_4($Fe^{2+}Cr_{2-x}Fe_x^{3+}O_4$). *J. Phys. Chem. Solids* **1971**, *32*, 717−729.

(3) Chambers, S. A.; Droubay, T. C.; Kaspar, T. C.; Nayyar, I. H.; McBriarty, M. E.; Heald, S. M.; Keavney, D. J.; Bowden, M. E.; Sushko, P. V. Electronic and Optical Properties of a Semiconducting Spinel (Fe_2CrO_4). *Adv. Funct. Mater.* **2017**, *27*, 1605040.

(4) Scafetta, M. D.; Yang, Z.; Spurgeon, S. R.; Bowden, M. E.; Kaspar, T. C.; Heald, S. M.; Chambers, S. A. Epitaxial Growth and

Atomic Arrangement in Fe $_2$ CrO $_4$ on Crystal Symmetry Matched (001) $MgAl_2O_4$. *J. Vac. Sci. Technol., A* **2019**, *37*, 031511.
(5) Scafetta, M. D.; May, S. J. Effect of Cation Off-Stoichiometry on Optical Absorption in Epitaxial $LaFeO_3$ Films. *Phys. Chem. Chem. Phys.* **2017**, *19*, 10371−10376.
(6) Smolin, S. Y.; Scafetta, M. D.; Choquette, A. K.; Sfeir, M. Y.; Baxter, J. B.; May, S. J. Static and Dynamic Optical Properties of $La_{1-x}Sr_xFeO_{3-\delta}$: The Effects of A-Site and Oxygen Stoichiometry. *Chem. Mater.* **2016**, *28*, 97−105.
(7) Scafetta, M. D.; Xie, Y. J.; Torres, M.; Spanier, J. E.; May, S. J. Optical Absorption in Epitaxial $La_{1-x}Sr_xFeO_3$ Thin Films. *Appl. Phys. Lett.* **2013**, *102*, 081904.
(8) Özdemir, Ö.; Dunlop, D. J.; Moskowitz, B. M. The Effect of Oxidation on the Verwey Transition in Magnetite. *Geophys. Res. Lett.* **1993**, *20*, 1671−1674.
(9) Parkinson, G. S. Iron Oxide Surfaces. *Surf. Sci. Rep.* **2016**, *71*, 272−365.
(10) Chen, J.; Shen, M.; Wang, X.; Qi, G.; Wang, J.; Li, W. The Influence of Nonstoichiometry on $LaMnO_3$ Perovskite for Catalytic NO Oxidation. *Appl. Catal., B* **2013**, *134*−*135*, 251−257.
(11) Töpfer, J.; Goodenough, J. B. $LaMnO_{3+\delta}$ Revisited. *J. Solid State Chem.* **1997**, *130*, 117−128.
(12) McClure, D. S. The Distribution of Transition Metal Cations in Spinels. *J. Phys. Chem. Solids* **1957**, *3*, 311−317.
(13) Yearian, H. J.; Kortright, J. M.; Langenheim, R. H. Lattice Parameters of the $FeFe_{2-x}Cr_xO_4$ Spinel System. *J. Chem. Phys.* **1954**, *22*, 1196−1198.
(14) Nasrazadani, S.; Raman, A. The Application of Infrared Spectroscopy to the Study of Rust Systems—II. Study of Cation Deficiency in Magnetite (Fe_3O_4) Produced during Its Transformation to Maghemite (γ-Fe_2O_3) and Hematite (α-Fe_2O_3). *Corros. Sci.* **1993**, *34*, 1355−1365.
(15) Chamberlin, S. E.; Wang, Y.; Lopata, K.; Kaspar, T. C.; Cohn, A. W.; Gamelin, D. R.; Govind, N.; Sushko, P. V.; Chambers, S. A. Optical Absorption and Spectral Photoconductivity in α-$(Fe_1$-$xCrx)_2O_3$ Solid-Solution Thin Films. *J. Phys.: Condens. Matter* **2013**, *25*, 392002.
(16) Kaspar, T. C.; Chamberlin, S. E.; Bowden, M. E.; Colby, R.; Shutthanandan, V.; Manandhar, S.; Wang, Y.; Sushko, P. V.; Chambers, S. A. Impact of Lattice Mismatch and Stoichiometry on the Structure and Bandgap of $(Fe,Cr)_2O_3$ Epitaxial Thin Films. *J. Phys.: Condens. Matter* **2014**, *26*, 135005.
(17) Jonker, G. Semiconducting Properties of Mixed Crystals with Perovskite Structure. *Physica* **1954**, *3*, 1118−1122.
(18) Piovano, A.; Agostini, G.; Frenkel, A. I.; Bertier, T.; Prestipino, C.; Ceretti, M.; Paulus, W.; Lamberti, C. Time Resolved in Situ XAFS Study of the Electrochemical Oxygen Intercalation in $SrFeO_{2.5}$ Brownmillerite Structure: Comparison with the Homologous SrCoO2.5 System. *J. Phys. Chem. C* **2011**, *115*, 1311−1322.
(19) Wang, L.; Du, Y.; Sushko, P. V.; Bowden, M. E.; Stoerzinger, K. A.; Heald, S. M.; Scafetta, M. D.; Kaspar, T. C.; Chambers, S. A. Hole-Induced Electronic and Optical Transitions in $La_{1-x}Sr_xFe\ O_3$ Epitaxial Thin Films. *Phys. Rev. Mater.* **2019**, *3*, 025401.
(20) Blasco, J.; Aznar, B.; García, J.; Subías, G.; Herrero-Martín, J.; Stankiewicz, J. Charge Disproportionation in $La_{1-x}Sr_xFeO_3$ Probed by Diffraction and Spectroscopic Experiments. *Phys. Rev. B: Condens. Matter Mater. Phys.* **2008**, *77*, 054107.
(21) Chen, J. Y. C.; Dang, L.; Liang, H.; Bi, W.; Gerken, J. B.; Jin, S.; Alp, E. E.; Stahl, S. S. Operando Analysis of NiFe and Fe Oxyhydroxide Electrocatalysts for Water Oxidation: Detection of Fe 4+ by Mössbauer Spectroscopy. *J. Am. Chem. Soc.* **2015**, *137*, 15090−15093.
(22) Forslund, R. P.; Hardin, W. G.; Rong, X.; Abakumov, A. M.; Filimonov, D.; Alexander, C. T.; Mefford, J. T.; Iyer, H.; Kolpak, A. M.; Johnston, K. P.; et al. Exceptional Electrocatalytic Oxygen Evolution via Tunable Charge Transfer Interactions in $La_{0.5}Sr_{1.5}Ni_{1-x}Fe_xO_{4\pm\delta}$ Ruddlesden-Popper Oxides. *Nat. Commun.* **2018**, *9*, 3150.
(23) Streltsov, S. S.; Shorikov, A. O.; Skornyakov, S. L.; Poteryaev, A. I.; Khomskii, D. I. Unexpected 3+ Valence of Iron in FeO_2, a Geologically Important Material Lying "in between" Oxides and Peroxides. *Sci. Rep.* **2017**, *7*, 13005.
(24) Xie, Y. J.; Scafetta, M. D.; Moon, E. J.; Krick, A. L.; Sichel-Tissot, R. J.; May, S. J. Electronic Phase Diagram of Epitaxial $La_{1-x}Sr_xFeO_3$ Films. *Appl. Phys. Lett.* **2014**, *105*, 062110.
(25) Liu, M.; Hoffman, J.; Wang, J.; Zhang, J.; Nelson-Cheeseman, B.; Bhattacharya, A. Non-Volatile Ferroelastic Switching of the Verwey Transition and Resistivity of Epitaxial Fe_3O_4/PMN-PT (011). *Sci. Rep.* **2013**, *3*, 1876.
(26) Liu, X. H.; Rata, A. D.; Chang, C. F.; Komarek, A. C.; Tjeng, L. H. Verwey Transition in Fe_3O_4 Thin Films: Influence of Oxygen Stoichiometry and Substrate-Induced Microstructure. *Phys. Rev. B: Condens. Matter Mater. Phys.* **2014**, *90*, 125142.
(27) Scafetta, M. D.; Cordi, A. M.; Rondinelli, J. M.; May, S. J. Band Structure and Optical Transitions in $LaFeO_3$: Theory and Experiment. *J. Phys.: Condens. Matter* **2014**, *26*, 505502.
(28) Lenaz, D.; Skogby, H.; Princivalle, F.; Halenius, U. Structural Changes and Valence States in the $MgCr_2O_4$-$FeCr_2O_4$ Solid Solution Series. *Phys. Chem. Miner.* **2004**, *31*, 633−642.
(29) Hålenius, U.; Skogby, H.; Andreozzi, G. B. Influence of Cation Distribution on the Optical Absorption Spectra of Fe 3+ -Bearing Spinel s.s. -Hercynite Crystals: Evidence for Electron Transitions in VI Fe 2+ - VI Fe 3+ Clusters. *Phys. Chem. Miner.* **2002**, *29*, 319−330.
(30) Smith, G. Evidence for Absorption by Exchange-Coupled Fe2+-Fe3+ Pairs in the near Infra-Red Spectra of Minerals. *Phys. Chem. Miner.* **1978**, *3*, 375−383.
(31) Mattson, S. M.; Rossman, G. R. Identifying Characteristics of Charge Transfer Transitions in Minerals. *Phys. Chem. Miner.* **1987**, *14*, 94−99.
(32) Mattson, S. M.; Rossman, G. R. Fe2+-Fe3+ Interactions in Tourmaline. *Phys. Chem. Miner.* **1987**, *14*, 163−171.
(33) Balberg, I.; Pinch, H. L. The Optical Absorption of Iron Oxides. *J. Magn. Magn. Mater.* **1978**, *7*, 12−15.
(34) Flesch, H.-G.; Werzer, O.; Weis, M.; Jakabovič, J.; Kováč, J.; Haško, D.; Jakopič, G.; Wondergem, H. J.; Resel, R. A Combined X-Ray, Ellipsometry and Atomic Force Microscopy Study on Thin Parylene-C Films. *Phys. Status Solidi A* **2009**, *206*, 1727−1730.
(35) Solina, D. M.; Cheary, R. W.; Lupscha, F. A.; Swift, P. D. An Investigation of Metal Thin Films Using X-Ray Reflectivity and Atomic Force Microscopy. *Adv. X-Ray Anal.* **1997**, *40*.
(36) Lee, C.-H.; Podraza, N. J.; Zhu, Y.; Berger, R. F.; Shen, S.; Sestak, M.; Collins, R. W.; Kourkoutis, L. F.; Mundy, J. A.; Wang, H.; et al. Effect of Reduced Dimensionality on the Optical Band Gap of $SrTiO_3$. *Appl. Phys. Lett.* **2013**, *102*, 122901.
(37) Gao, Y.; Chambers, S. A. Heteroepitaxial Growth of α-Fe_2O_3, γ-Fe_2O_3 and Fe_3O_4 Thin Films by Oxygen-Plasma-Assisted Molecular Beam Epitaxy. *J. Cryst. Growth* **1997**, *174*, 446−454.
(38) Gao, Y.; Kim, Y. J.; Chambers, S. A. Preparation and Characterization of Epitaxial Iron Oxide Films. *J. Mater. Res.* **1998**, *13*, 2003−2014.
(39) Droubay, T.; Rosso, K. M.; Heald, S. M.; Mccready, D. E.; Wang, C. M.; Chambers, S. A. Structure, Magnetism, and Conductivity in Epitaxial Ti-Doped a-Fe_2O_3 Hematite: Experiment and Density Functional Theory Calculations. *Phys. Rev. B: Condens. Matter Mater. Phys.* **2007**, *75*, 104412.
(40) Kaspar, T. C.; Chamberlin, S. E.; Chambers, S. A. Surface Structure of α-Cr_2O_3(0001) after Activated Oxygen Exposure. *Surf. Sci.* **2013**, *618*, 159−166.
(41) Domenichini, B.; Amilain-Basset, K.; Bourgeois, S. Dynamic Segregation during Ferrite Oxidation Revealed by XPS. *Surf. Interface Anal.* **2002**, *34*, 527−530.
(42) Qiao, L.; Droubay, T. C.; Varga, T.; Bowden, M. E.; Shutthanandan, V.; Zhu, Z.; Kaspar, T. C.; Chambers, S. A. Epitaxial Growth, Structure, and Intermixing at the $LaAlO_3$/$SrTiO_3$ Interface as the Film Stoichiometry Is Varied. *Phys. Rev. B: Condens. Matter Mater. Phys.* **2011**, *83*, 85408.

https://dx.doi.org/10.1021/acsomega.9b03299
ACS Omega 2020, 5, 3240−3249

(43) Kendelewicz, T.; Kaya, S.; Newberg, J. T.; Bluhm, H.; Mulakaluri, N.; Moritz, W.; Scheffler, M.; Nilsson, A.; Pentcheva, R.; Brown, G. E. X-Ray Photoemission and Density Functional Theory Study of the Interaction of Water Vapor with the Fe_3O_4 (001) Surface at Near-Ambient Conditions. *J. Phys. Chem. C* **2013**, *117*, 2719−2733.
(44) Cornell, R. M.; Schwertmann, U. *The Iron Oxides*; Wiley-VCH Verlag GmbH & Co. KGaA: Weinheim, FRG, 2003; Vol. *6*.
(45) Ohgushi, K.; Okimoto, Y.; Ogasawara, T.; Miyasaka, S.; Tokura, Y. Magnetic, Optical, and Magnetooptical Properties of Spinel-Type ACr_2X_4(A = Mn, Fe, Co, Cu, Zn, Cd; X = O, S, Se). *J. Phys. Soc. Jpn.* **2008**, *77*, 034713.
(46) Frederikse, H. P. R. Elastic Constants of Single Crystals. In *CRC Handbook of Chemistry and Physics: A Ready-reference Book of Chemistry and Physics*; Lide, D. R., Ed.; CRC Press, 2003; p 37.
(47) Guo, H.; Barnard, A. S. Modeling the Iron Oxides and Oxyhydroxides for the Prediction of Environmentally Sensitive Phase Transformations. *Phys. Rev. B: Condens. Matter Mater. Phys.* **2011**, *83*, 094112.
(48) Droubay, T.; Chambers, S. Surface-Sensitive Fe 2p Photoemission Spectra for α-Fe_2O_3(0001): The Influence of Symmetry and Crystal-Field Strength. *Phys. Rev. B: Condens. Matter Mater. Phys.* **2001**, *64*, 205414.
(49) Kocsis, V.; Bordács, S.; Varjas, D.; Penc, K.; Abouelsayed, A.; Kuntscher, C. A.; Ohgushi, K.; Tokura, Y.; Kézsmárki, I. Magnetoelasticity inACr2O4spinel oxides (A=Mn, Fe, Co, Ni, and Cu). *Phys. Rev. B: Condens. Matter Mater. Phys.* **2013**, *87*, 064416.
(50) Schrettle, F.; Kant, C.; Lunkenheimer, P.; Mayr, F.; Deisenhofer, J.; Loidl, A. Wüstite: Electric, Thermodynamic and Optical Properties of FeO. *Eur. Phys. J. B* **2012**, *85*, 164.
(51) Gasparov, L. V.; Tanner, D. B.; Romero, D. B.; Berger, H.; Margaritondo, G.; Forró, L. Infrared and Raman Studies of the Verwey Transition in Magnetite. *Phys. Rev. B: Condens. Matter Mater. Phys.* **2000**, *62*, 7939−7944.
(52) Kocsis, V.; Bordács, S.; Deisenhofer, J.; Kiss, L. F.; Ohgushi, K.; Kaneko, Y.; Tokura, Y.; Kézsmárki, I. Strong Magneto-Optical Effects in ACr_2O_4 (A = Fe, Co) Spinel Oxides Generated by Tetrahedrally Coordinated Transition Metal Ions. *Phys. Rev. B* **2018**, *97*, 125140.
(53) Sugano, S. *Multiplets of Transition-Metal Ions in Crystals*; Academic Press: Cambridge, MA, 1970.
(54) Della Giusta, A.; Princivalle, F.; Carbonin, S. Crystal Structure and Cation Distribution in Some Natural Magnetites. *Mineral. Petrol.* **1987**, *37*, 315−321.

https://dx.doi.org/10.1021/acsomega.9b03299
ACS Omega 2020, 5, 3240−3249